Grain Boundary Facilitated Dissolution of Nanocrystalline NpO$_2$(s) from Legacy Waste Processing

SCHOLARONE™
Manuscripts

Environmental Significance Statement

Prediction of environmental fate of nuclear materials for geologic disposal of spent nuclear fuel and management of legacy nuclear waste poses a complex challenge. Actinide oxides, $AnO_2(s)$ (An = Th, U, Np, Pu), are thermodynamically stable and likely to represent the source term in subsurface disposal scenarios, particularly into the far-field. Dissolution mechanisms must be clearly understood to support robust predictions. Previous work demonstrated that $AnO_2(s)$ may inherently form nanocrystalline phases which can alter solubility and environmental mobility from $AnO_2(s)$ through processes such as colloidal transport. In this work, $NpO_2(s)$ produced through legacy nuclear waste processing is dissolved under vadose zone conditions, revealing that both aqueous and colloidal Np emanate from the initial nanocrystalline material. Findings could alter conceptual models for mobility from $AnO_2(s)$ in the environment.

Grain Boundary Facilitated Dissolution of Nanocrystalline NpO$_2$(s) from Legacy Waste Processing

Kathryn M. Peruski[(1)], *Kelliann C. Koehler*[(2)], *Brian A. Powell*[(1,3,4)*]

[(1)]Environmental Engineering and Earth Sciences, Clemson University, Anderson, SC,

US 29625

[(2)] Clemson Electron Microscopy Facility, Division of Research, Clemson University,

Anderson, SC, US 29625

[(3)]Department of Chemistry, Clemson University, Clemson, SC USA 29634

[(4)]Savannah River National Laboratory, Aiken, SC, USA 29808

KEYWORDS: Neptunium, dissolution, grain boundary, colloids, actinides

1
2
3
4
5
6
7
8
9
10
11
12
13
14
15
16
17
18
19
20
21
22
23
24
25
26
27
28
29
30
31
32
33
34
35
36
37
38
39
40
41
42
43
44
45
46
47
48
49
50
51
52
53
54
55
56
57
58
59
60

ABSTRACT

Dissolution of actinide dioxides, including neptunium dioxide ($NpO_2(s)$), is paramount for prediction of environmental fate of nuclear materials. Quantifying dissolution rates, as well as understanding qualitative dissolution mechanisms, informs performance assessment for geologic disposal of spent nuclear fuel and management of legacy radioactive waste. The aim of this research was to measure the dissolution rate of nanocrystalline $NpO_2(s)$, produced through legacy nuclear waste processing, under oxidizing conditions, as well as to characterize surface alteration to the material. The solid phase was characterized using electron microscopy techniques (SEM/STEM) and x-ray photoelectron spectroscopy (XPS), indicating preferential dissolution of Np-hydroxide contained in the grain boundaries of $NpO_2(s)$ and fragmentation of grains from

2

the matrix. The oxidative dissolution was monitored over 40 weeks, yielding a two-step

kinetic dissolution model involving hydration of $NpO_2(s)$ and subsequent oxidation and

dissolution of the hydroxide phase. The proposed dissolution models for nanocrystalline

$NpO_2(s)$ suggest that microstructural features such as grain boundaries are key factors

affecting dissolution, including release of colloidal particles, and ultimately, environmental

fate and transport of nuclear materials.

Introduction

Neptunium (Np) is a man-made, radioactive element found in a variety of

processes in the nuclear fuel cycle. One of the most critical Np isotopes is [237]Np because

of its long-lived nature (half-life of 2.144 million years) and subsequent potential for long-

term environmental persistence. Neptunium also has the potential for high environmental

mobility, dependent on oxidation state.   [237]Np is found in spent nuclear fuel[1] from

commercial power production and is also part of the legacy waste stream from United

States nuclear weapons production. The U.S. Department of Energy (DOE) Savannah

River Site (SRS) produces neptunium dioxide (NpO_2(s)) through an oxalate precipitation

and calcination process for purification, stabilization, and eventual use in the production

of Pu-238[2-4]. Estimates of total DOE production of Np exceed 1-2 tons, with SRS holding

294 kg of Np as of 1998[5].

Geologic disposal of spent nuclear fuel from commercial nuclear reactors is being

considered and implemented in numerous countries around the world[6], necessitating

thorough prediction of environmental degradation of solid phases relevant to spent fuel

for performance assessment and policy decisions. While the main constituent of spent

nuclear fuel is uranium dioxide (UO_2(s)), burnup produces other actinide oxide phases,

such as NpO_2(s) and PuO_2(s), which can be found as substitutions in the fuel grain

matrix[1, 7]. Actinide oxides, such as NpO_2(s), are profoundly insoluble under reducing

conditions[8, 9], thus limiting environmental mobility of actinides. However, under common

environmental conditions, Np can undergo redox reactions, which alters solubility and

environmental mobility. Under oxidizing conditions, Np forms the neptunyl dioxycation

(NpO_2^+), which is extremely soluble and mobile (relative to Np(IV) aqueous ion) in

environmental waters and sediment[10-13]. Prediction of oxidation of $NpO_2(s)$ to the more

mobile, oxidized species is therefore important for thorough environmental assessment.

Potential alteration and dissolution of spent nuclear fuel in a geologic repository due to

presence of oxidizing sources, such as peroxide, oxygen gas, or oxidizing groundwater

could result in significant environmental contamination[1, 7]. The potential mobility of NpO_2^+

has been recognized as an important factor in risk assessment for geologic disposal of

spent nuclear fuel, with emphasis on Np(V) solubility and speciation in environmental

waters[10], retardation of Np(V) aqueous species in sediment[14, 15], and reactive transport

modeling of Np at potential disposal sites[16].   Specific environmental dissolution and

transport studies of $NpO_2(s)$ sources in the vadose zone (oxidizing conditions) found

mobile ionic and colloidal Np species emanating from $NpO_2(s)$ sources[17], which suggest

$NpO_2(s)$ dissolution is a complex process and supports the need for laboratory-scale

oxidizing dissolution studies to confirm dissolution rate and mechanism in a more

controlled setting.

Previous $NpO_2(s)$ dissolution studies have focused on strict reducing conditions and measurement of total aqueous solubility. Early studies explored solubility of Np(IV) hydrous oxide in acidic[18] and alkaline conditions[19, 20] relevant to proposed geologic repositories. Much of the data collected on Np in these studies is at or below aqueous detection limits due to instrumental detection limits of the time. Neck *et al.*[21] were able to achieve better detection limits for Np by using advanced absorption spectroscopy techniques. Data in these studies are generated from a Np (IV) hydrous oxide solid, precipitated through a rapid neutralization of acidic Np(IV) solution, rather than crystalline $NpO_2(s)$. To produce Np(IV) hydrous oxide, NaOH is rapidly added to Np(IV) solution in $HClO_4$ or HCl to adjust pH to 8-10, or as high as 12, producing a solid precipitate that is rarely characterized outside of powder x-ray diffraction[20-23]. A more recent study by Kim *et al.*[24] does report the solubility of crystalline $NpO_2(s)$, rather than a hydrous oxide, but the work is site-specific to the Korean test site for geologic disposal under reducing, alkaline conditions and reports that Np(IV) hydroxide and carbonate aqueous species are the primary aqueous species. The few studies of oxidative dissolution of $NpO_2(s)$ do not present dissolution rates and present limited data describing the characterization of the

6

solid phases[22, 23, 25]. The specific solid phase used in a dissolution study is highly important, given that reported solubility values vary by orders of magnitude between crystalline $NpO_2(s)$ and amorphous Np hydroxide[8, 9].

A key gap in existing $NpO_2(s)$ dissolution data is a thorough understanding of the dissolution reaction at the solid-water interface, including characterization of surface alteration and presentation of mechanistic dissolution models. The impact of solid phase microstructures, especially grain boundaries, on dissolution processes has been recognized for $UO_2(s)$ with relation to spent nuclear fuel. Dissolution has been shown to occur primarily at the grain boundaries, forming large channels within the fuel matrix[26-29], and under oxidizing conditions, forming secondary phases at the grain boundaries[30]. Grain boundaries are considered to be highly reactive and primary sites of dissolution processes, as evidenced by work with nanocrystalline $CeO_2(s)$[31, 32] and $ThO_2(s)$[33], but the role of such microstructures has not been evaluated for transuranic (Np, Pu) oxides. Therefore, the objective of this work is to 1) measure the oxidative dissolution rate of nanocrystalline $NpO_2(s)$ and 2) characterize surface alteration to the solid phase.

Through aqueous dissolution data as well as a suite of surface characterization, we find that nanocrystalline $NpO_2(s)$ undergoes a two-step grain boundary facilitated dissolution, producing both ionic and colloidal Np in solution. The high-resolution characterization of the surface of $NpO_2(s)$, along with conceptual and kinetic dissolution models, provide new insight into the fate of $NpO_2(s)$ in environmental conditions to inform performance assessment for long-term environmental fate of spent nuclear fuel and remediation of legacy nuclear waste contamination.

Methods

NpO₂(s) Dissolution

Approximately 5 mg of $NpO_2(s)$ was dissolved in triplicate in 20mL of a simulated pore water from Savannah River Site[34] (SI Table 1) at an initial pH 5.02. Dissolution experiments were mixed on an orbital shaker at 90 rpm at 25°C for the duration of the experiment. 20 μL aliquot and were taken at each time point over the 10 month-duration

of the experiment, diluted to 2 mL in deionized water, and centrifuged for 10 minutes at

8000 rpm in a Beckman Coulter C1015 fixed-angle rotor to remove particles >100nm

according to Stoke's Law[35]. 1 mL of sample was filtered using a Pall centrifuge filter

(10kDa MWCO), while the remaining sample was reserved as unfiltered. Both filtered

and unfiltered sample were diluted with 2% HNO_3 for inductively-coupled plasma mass

spectrometry (ICP-MS) analysis for ^{237}Np concentration in the aqueous phase. The

minimum detectable concentration (MDC) for ^{237}Np was 8×10^{-13} M. E_h and pH were

monitored throughout the experiment but were not adjusted. At the completion of the

experiment, remaining solid was separated, dried, and weighed to determine final mass

of $NpO_2(s)$.

$NpO_2(s)$ Characterization

        The $NpO_2(s)$, obtained from Savannah River National Laboratory, was

synthesized by oxalate precipitation and subsequent calcination to approximately 650°C

as part of testing for the HB-line process[2, 3]. Upon receipt at Clemson University,

1
2
3
4
5
6
7
8
9
10
11
12
13
14
15
16
17
18
19
20
21
22
23
24
25
26
27
28
29
30
31
32
33
34
35
36
37
38
39
40
41
42
43
44
45
46
47
48
49
50
51
52
53
54
55
56
57
58
59
60

NpO_2(s) was stored in a vinyl anerobic chamber (Coy Laboratory Products, <1 ppm

O_2(g), 1.5% H_2(g)) and rinsed with degassed deionized water for 48 hours prior to

further analysis. Solid was then suspended in a small amount of ethanol and divided

into aliquots for dissolution experiments and solid phase characterization. NpO_2(s) was

characterized using scanning electron microscopy (SEM), scanning transmission

electron microscopy (STEM), and X-ray photoelectron spectroscopy (XPS). Small

amounts of the solid phase were sampled during and after dissolution experiment for

characterization using the same techniques. Prior to shipment to Clemson University,

NpO_2(s) was analyzed by powder x-ray diffraction (PXRD) at Savannah River National

Laboratory to confirm crystallinity and composition of the material (SI Figure S1). The

NpO_2(s) obtained from Savannah River National Laboratory was also characterized

using x-ray absorption spectroscopy (XAS) as part of a previous study[17].

Samples were prepared for SEM by transferring solid onto double-sided carbon

tape on an aluminum stub. Samples were not sputter coated prior to analysis. Scanning

electron micrographs were taken on a Hitachi S4800 high resolution scanning electron

10

microscope with an accelerating voltage of 15kV and a working distance of 10 mm. Samples

were prepared for STEM (Hitachi HD2000 STEM, accelerating voltage 200kV) by casting 3 μL

of NpO$_2$(s) suspended in ethanol onto a copper-coated lacey carbon grid (300 mesh). Excess

liquid was blotted from the grid using a Kim wipe and grids were allowed to dry, covered in a

fume hood, for 24 hours prior to analysis.

Samples were prepared for XPS by first suspending a small amount of NpO$_2$(s) in

ethanol. Samples were embedded at the surface of a thermoplastic adhesive (TempFix Mounting

Adhesive) by heating a 6x6x1 mm aluminum mounting plate on a hot plate to 120°C, melting a

small amount of resin onto the aluminum, then allowing it to cool for approximately 5 minutes

before pipetting 3 μL of the suspension of NpO$_2$(s) onto the surface of the resin. The sample was

removed from the hot plate, allowed to cool for 24 hours, then cleaned with a Kim Wipe and

ethanol to remove any loose particles. Substrates were adhered to the platen using carbon tape

and an aluminum mask. The XPS data for Np samples was collected via PHI Versa Probe III

with a monochromatic Al Kα X-ray source (hv = 1486.6 eV). The Al anode was powered at 25W

and 15 kV. The instrument was calibrated to Au and Ag metallic binding energy (BE) and

instrument base pressure was above 1 x 10^{-7} Torr. The analysis area size was 1000 x 1000 μm^2

scanned with a beam size of 100 μm in diameter. Charging was compensated with electron beam

charge neutralization. The binding energies were calibrated to the C 1s peak at 284.8 eV. For all

samples survey spectra were collected with a step size of 0.8 eV, dwell time of 50 ms, a pass

energy of 224 eV, and with three sweeps per spectra. The high-resolution spectra for Np 4f, C 1s,

and O1s were collected at 90 degrees with a pass energy of 140 eV, 0.125 eV step size, and a

dwell time of 100 ms. C 1s and O 1s were collected with 3 sweeps and 6 sweeps respectively. Np

4f spectra were collected with a pass with 30 sweeps due to low concentration of Np relative to C and O.

XPS peak fitting for Np 4f peaks was determined based on published actinide dioxide XPS literature[33, 36-38] and a series of controls including Np(IV) and Np(V) hydroxide samples run under the sample experimental protocol described above. Np(IV) and Np(V) hydroxide controls were prepared by rapid neutralization of acidic Np(IV) and Np(V) stocks, according to established methods by Strickert *et al.*[23] and Neck *et al.*[39], respectively. All spectra were first calibrated to carbon 1s signal at 284.8 eV. Peak fittings were modeled in Casa XPS. A U 2 Tougaard baseline was applied to all samples. Initial peak approximation model was based on analysis done by Vandenborre *et al.*[33] and Teterin *et al.*[36]. Peaks were then fit with the peak fitting parameters of SGL(60) and asymmetry factor T(1) and a FWHM of 1.75 eV for 7/2 and 5/2 peaks and 1.30 eV for satellite peaks within Casa. Based on the broadness of the $4f_{5/2}$ and $4f_{7/2}$ transitions as well as the described peak fitting parameters, the Np spectra was fit with two species resulting in two doublets, with two satellite peaks corresponding to $4f_{5/2}$ and $4f_{7/2}$ transitions, respectively. Fitting parameters were kept consistent across all samples and table of parameters is provided in Supporting Information (SI Table S2).

Results and Discussion

NpO$_2$(s) Dissolution

12

NpO$_2$(s) dissolution was monitored over the course of 40 weeks, showing a

change in dissolution rate over time and presence of a dissolved, filterable colloid

throughout the experiment. Dissolution proceeded rapidly over the first 4 weeks of the

experiment, then more gradually for the duration of the 40 weeks, reaching a maximum

^{237}Np aqueous concentration of 5 x 10^{-6} M (Figure 1). For all samples, less than 0.5%

of total solid dissolved. There was good agreement between triplicate samples, except

for one replicate which underwent a significant pH shift after 8 weeks (SI Figure S2).

The average pH of that replicate was 7.29 $\pm$ 0.81, whereas the other two replicates had

an average pH of 5.06 $\pm$ 0.37 over the course of 40 weeks. Given the unexplained pH

shift of one replicate after 8 weeks, subsequent data from this replicate was excluded

from averages presented in Figure 1. Across all samples, the average E$_h$ was 548.7 $\pm$

30.1 mV, indicating an oxidizing system. Filtered aqueous concentration of ^{237}Np was

consistently lower than unfiltered concentration (Figure 1), indicating the presence of a

filterable colloid being dissolved from the solid along with other aqueous ionic species.

The average filterable fraction of ^{237}Np during the dissolution experiment was 0.17 $\pm$

0.08 (SI Table S3). Filterable fractions above 0.1, even in the first days of the

13

experiment, indicate colloids were present soon after dissolution began. While the

filterable fraction varied throughout the experiment, the highest values were recorded

beyond 8 weeks, suggesting that the number of dissolved colloids increased over time.
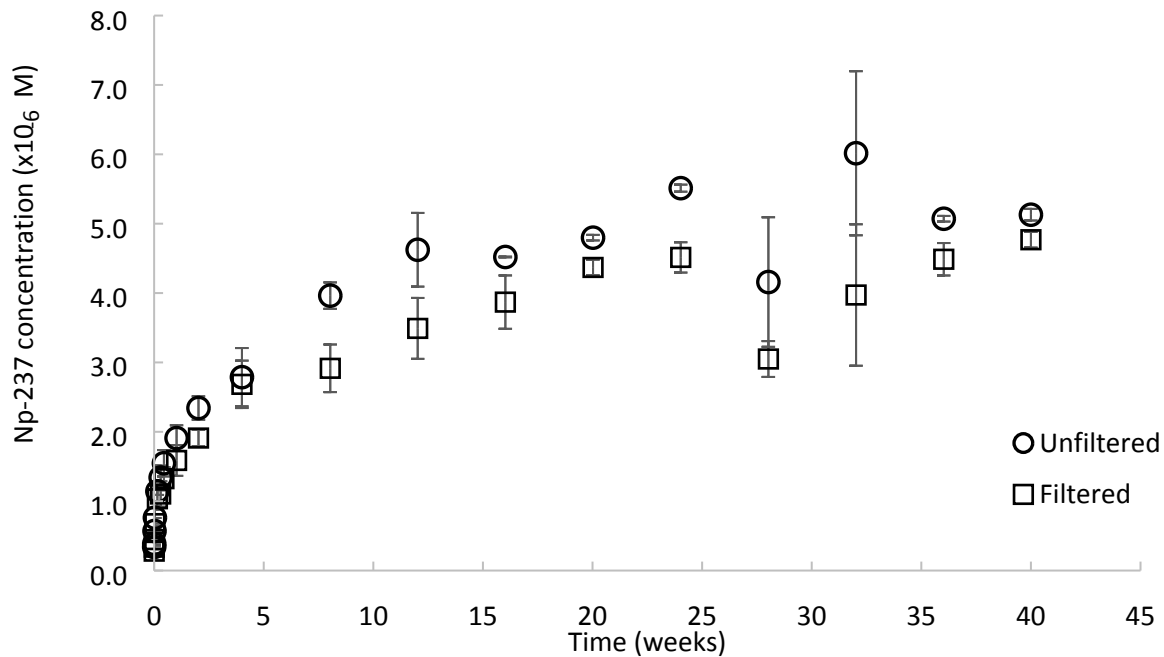
Figure 1. Average aqueous ^{237}Np concentration (M) as a function of dissolution time. Standard deviation from triplicate dissolution experiments, except >8 weeks, for which standard deviation is of duplicate samples.

NpO$_2$(s) Characterization

Electron micrographs showed that the as received NpO_2(s) was composed of

large aggregates with complex microstructure. Under low magnification, the NpO_2(s)

1
2
3
4
5
6
7
8
9
10
11
12
13
14
15
16
17
18
19
20
21
22
23
24
25
26
27
28
29
30
31
32
33
34
35
36
37
38
39
40
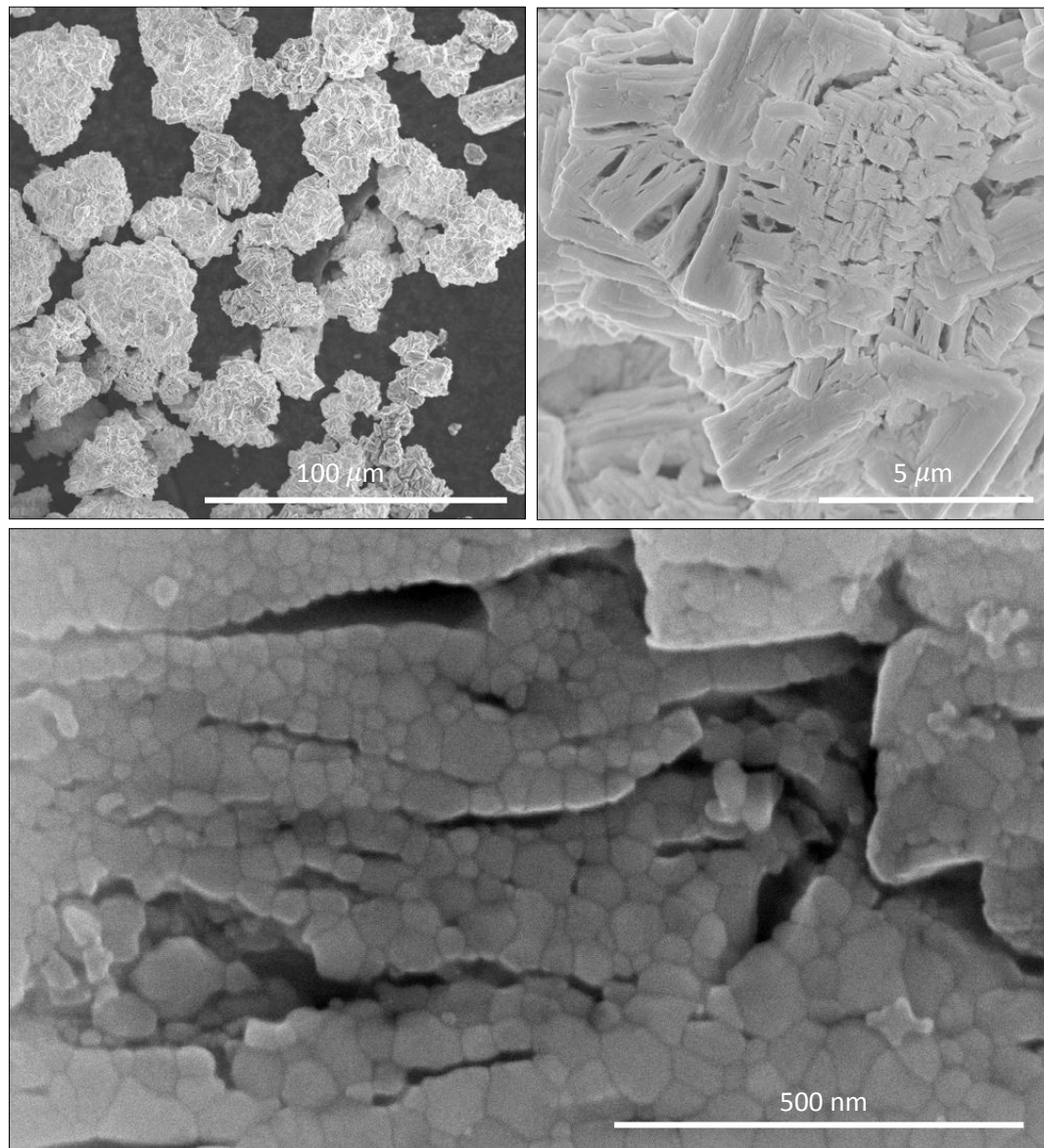41
42
43
44
45
46
47
48
49
50
51
52
53
54
55
56
57
58
59
60

appeared to be primarily composed of 10-50 μm aggregates (Figure 2, top left). Higher

magnification micrographs revealed that the aggregates were composed of platelets

(Figure 2, top right), which had distinct 10-50 nm grains and noticeable internal porosity

(Figure 2, bottom).

Figure 2. Scanning electron microscope images of $NpO_2(s)$ as received from SRNL at 3 different magnifications.

Micrographs of the solid phase during and after dissolution indicated preferential

dissolution at grain boundaries, resulting in breakdown of the aggregate structure. After

12 weeks of dissolution, micrographs of the solid phase showed rounding at the edges

of grains (SI Figure S3), suggesting that the material within the grain boundaries was

first to dissolve. Preferential grain boundary dissolution has been reported for similar

nanocrystalline oxide materials, such as $CeO_2(s)$[31, 32] and $ThO_2(s)$[33]. After 40 weeks of

dissolution, the material was primarily composed of smaller aggregates with significant

weathering and breakage (Figure 3, top row). The edges of the aggregate were jagged

and there was a large hole in the center of the aggregate (Figure 3, top left). There were

individual grains present on the surface of the material, seemingly not attached to the

primary matrix, as well as step features on the surface (Figure 3, top right) where

presumably entire sections of the matrix had been broken off. There were also

individual grains or small aggregates of 50-300 nm size present (Figure 3, bottom row)

along with the larger aggregates. These smallest aggregates were likely pieces that

had broken off of the larger structures during the dissolution process. The preferential

grain boundary dissolution may causes the matrix to lose cohesion as grain boundaries

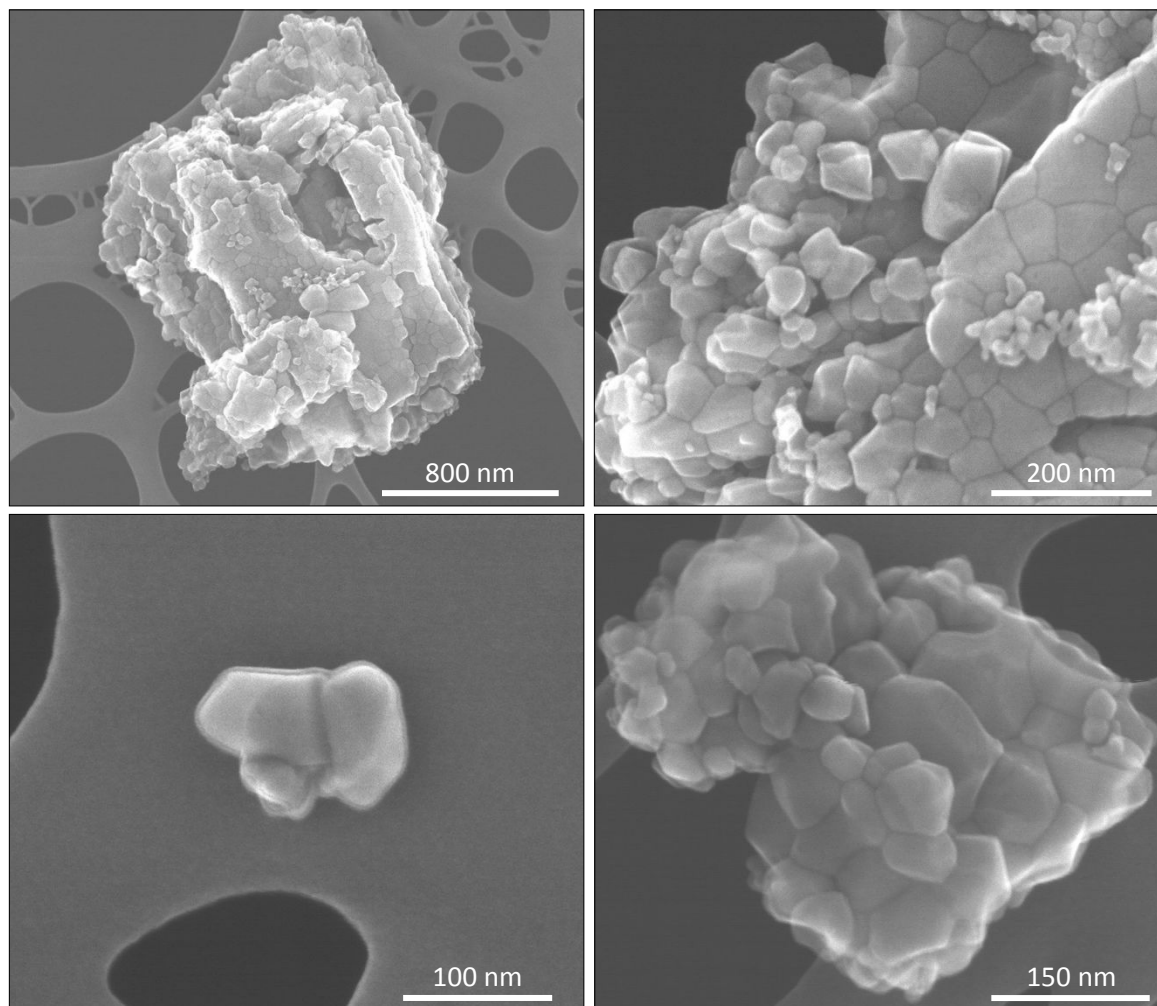are eroded, resulting in the release of individual grains or sections from the aggregate.

Figure 3. Scanning transmission electron microscope images of NpO_2(s) after 40 weeks of dissolution. Top row: large, partially dissolved aggregate (left) and higher magnification view of aggregate (right). Bottom row: smaller, isolated aggregates.

XPS investigation of the initial NpO_2(s) solid showed the Np 4f spectrum with expected spin-orbit split doublet ($4f_{7/2}$ and $4f_{5/2}$) and associated shake-up satellites

(Figure 4) and was best fit with 2 peaks (Peak 1, yellow and Peak 2, pink in Figure 4),

indicating the presence of two chemical environments for Np at the surface of NpO_2(s).

The distance between Peak 1 and Peak 2 was an average of 1.17 eV ± 0.15 eV (Table

1), making two peaks necessary for the fitting to avoid an excessively broad peak (~2ev),

as described in the Methods section. This significant peak separation in conjunction with

the total FWHM of the raw unfitted peak both indicate the presence of two species. Peak

1 (yellow) corresponds to NpO_2(s) when compared to published NpO_2(s) binding energy

(BE), peak-to-peak distance for the spin-orbit doublet, and satellite distances from Teterin

et al.[36] and Veal *et al.*[37]. Measured binding energies for the initial sample for Peak 1 are

within 0.5-0.6 eV of literature values[36, 37]. Slight shift in binding energy with respect to

published values can be attributed to a variety of factors, including sample charging,

particle size effects, or differences in instrumentation. Peak-to-peak distance ($4f_{7/2}$ to

$4f_{5/2}$) in the initial sample was 11.64 eV, which agrees well with 11.7 eV reported in Teterin

et al. Satellite distances for Peak 1 are 6.78 eV and 6.85 eV for $4f_{7/2}$ and $4f_{5/2}$,

respectively, compared to 6.9 eV from Teterin *et al.*[36]. Full list of BE provided in Table 1

and a representative survey spectrum is provided in Supporting Information (SI Figure

S5). Given the agreement between Peak 1 (yellow) spectrum and published $NpO_2(s)$

literature, Peak 1 is attributed to $NpO_2(s)$ and will be referred to subsequently as the oxide

phase. Peak 2 corresponds to a second chemical environment of Np, which is proposed

to be a hydroxide phase. Published data on Np(IV) hydroxide or hydrated phases are not

available, but a similar second chemical environment was proposed for $ThO_2(s)$ by

Vandenborre *et al.*[33], and the slight influence of hydroxide or hydrated phases is also

noted for $NpO_2(s)$ by Teterin *et al.*[36].

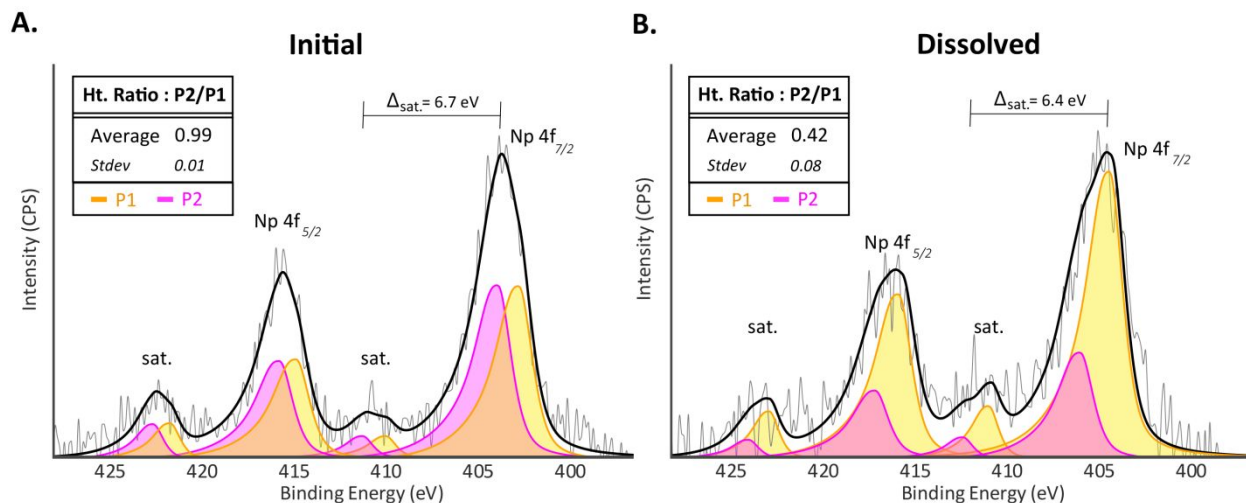**Figure 4.** X-ray photoelectron spectroscopy 4f spectra for $NpO_2(s)$ before (left) and after (right) dissolution. Smoothed raw data shown in gray and fit envelope shown in black. For both spectra, Peak 1 shown in yellow and Peak 2 shown in pink.

The oxidation state of the sample was determined based on comparison to Np(IV) and

Np(V) controls. Published literature on Np oxidation state determination via XPS is limited but

suggests that satellite peaks are an appropriate means for oxidation state assignment[40]. More

extensive literature is available on uranium oxidation state assignment using XPS[41, 42], which

confirms that peak to satellite distance is the best method for oxidation state determination,

rather than the 4f binding energies. The measured distance to satellites of Np(IV) hydroxide and

Np(V) hydroxide control samples were 7.16 eV ± 0.34 eV and 10.07 eV ± 0.11 eV respectively

(SI Figure S4 & SI Table S4). Given the approximately 3 eV difference in satellite peak

location, the satellite distance was identified as the key marker for oxidation state of Np in the

samples. The average measured distance to satellites of the initial and dissolved samples were

6.7 eV ± 0.35 and 6.4 eV ± 0.45 eV, respectively, identifying these samples as Np(IV).

Measured BE, satellite distances, and Np 4f spectra for Np(IV) and Np(V) controls are provided

in Supporting Information. The absence of Np(V) solid phases both before and after

dissolution indicates that no oxidized Np phases precipitated during dissolution, but

rather, that Np(V) forming on the surface rapidly desorbs into solution (i.e., any oxidized

Np remains in solution).

Table 1. X-ray photoelectron spectroscopy peak and satellite binding energies for initial
and dissolved $NpO_2(s)$ samples.

Sample		Binding Energy (eV)								Distance P1 to P2
		Peak 1 $4f_{7/2}$	Peak 2 $4f_{7/2}$	Sat 1 $4f_{7/2}$	Sat 2 $4f_{7/2}$	Peak 1 $4f_{5/2}$	Peak 2 $4f_{5/2}$	Sat1 $4f_{5/2}$	Sat 2 $4f_{5/2}$	Δ1-2 (eV)
Initial	Avg.	402.93	404.09	409.67	410.77	414.68	415.66	421.49	422.52	1.17
	StDev	0.06	0.08	0.49	0.27	0.15	0.10	0.28	0.29	0.15
Dissolved	Avg.	404.20	405.93	410.54	412.34	415.72	417.26	422.12	423.85	1.73
	StDev	0.48	0.32	0.58	0.94	0.61	0.66	0.35	0.31	0.17

Comparing the initial solid to the dissolved solid, a change in the P1/P2 ratio indicates a preferential dissolution of the hydroxide phase at the surface of the solid. The ratio of Peak 1 (oxide) to Peak 2 (hydroxide), shown as inset in Figure 4, was calculated to understand the change in the sample between the initial and dissolved material. Based on the peak fitting, there is a clear shift in material composition evident from the decrease in Peak 2 relative to Peak 1 between the initial and dissolved materials (Figure 4). The calculated peak ratios (P2/P1) for initial and dissolved materials were 0.99 ± 0.01 and 0.42 ± 0.08, respectively. This represents a shift from approximately a 1:1 ratio of hydroxide to oxide for initial solid to a 1:2 ratio of hydroxide to oxide for the dissolved solid at the surface of the material, indicating a significant loss of the hydroxide phase that was initially present with respect to the oxide phase. The XPS data provide relative proportions of these two species at the surface of the solid, but do not represent bulk composition. Powder x-ray diffraction data (SI Figure S1) confirms that the bulk material is $NpO_2(s)$. The hydroxide phase would be expected to be growing in on the surface of material, particularly in the grain boundaries, due to surface hydration during the dissolution process. However, the XPS data indicates a loss of hydroxide phase, suggesting that the dissolution rate of the hydroxide phase, which was present in some initial fraction, evidently is far greater than the ingrowth rate.

Dissolution Mechanism and Rate

From the aqueous and solid phase data, a conceptual model of the dissolution mechanism of nanocrystalline $NpO_2(s)$ is developed, asserting that grain boundaries are the primary point of the dissolution reaction (Figure 5). The nanocrystalline material contains both $NpO_2(s)$ and Np-hydroxide, shown in XPS data. The XPS results also indicate that an initial fraction of the

hydroxide phase on the surface of the solid is preferentially dissolved with respect to the oxide, despite expected ingrowth. Literature from $ThO_2(s)$ also proposes a conceptual model where $ThO_2(s)$ dissolves by preferential dissolution of a hydroxide phase[33]. Dissolution also preferentially occurs at the grain boundaries of $NpO_2(s)$, as evidenced by electron microscopy, and supported by $ThO_2(s)$[33] and $CeO_2(s)$ literature[31, 32], which note preferential grain boundary dissolution in nanocrystalline solids as well.
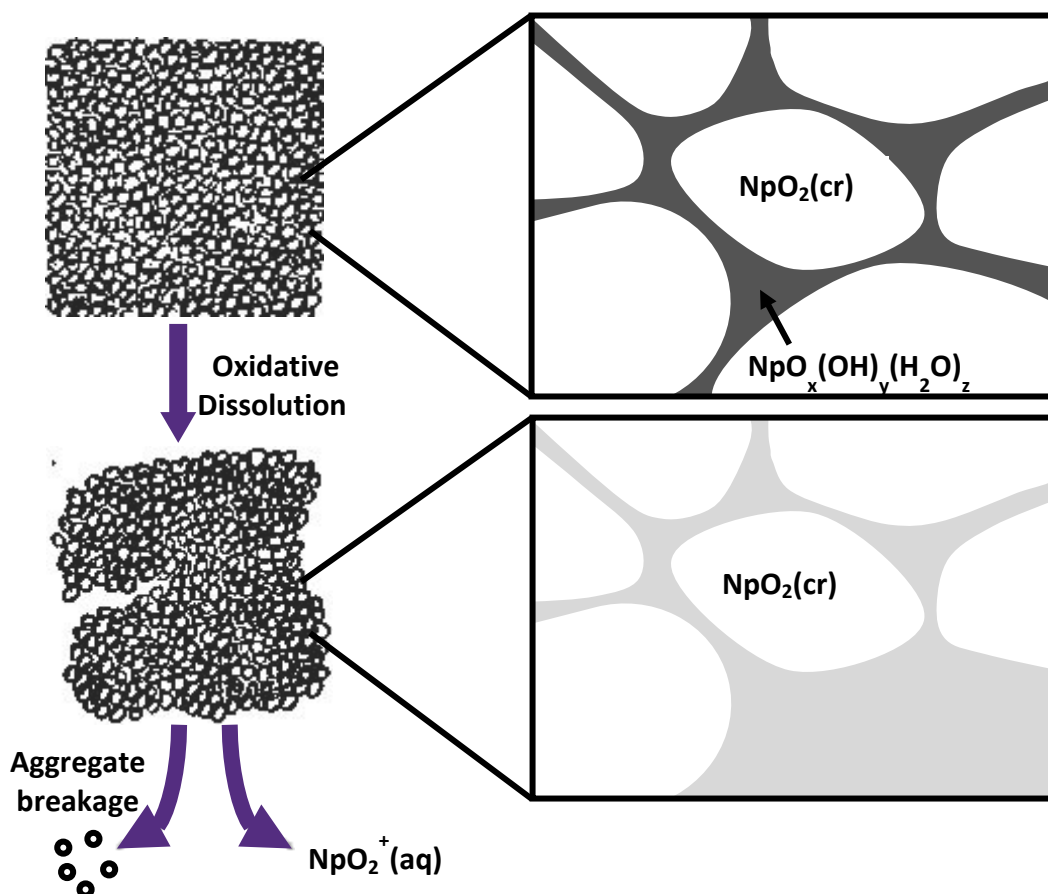

Figure 5. Conceptual model of nanocrystalline $NpO_2(s)$ dissolution mechanisms.

Comparison of filtered versus non-filtered samples in the batch dissolution studies

indicates the presence of colloids in solution. These colloids are likely individual

crystallites or small aggregates broken off from the nanocrystalline matrix, as shown by

electron microscopy. Aqueous phase data also demonstrates the presence of aqueous

ionic Np, which is presumed to be oxidized in the form of NpO_2^+ due to oxidizing aqueous

conditions. Overall, the $NpO_2(s)$ dissolution occurs primarily at the grain boundaries of

the nanocrystalline material, which contain a hydroxide phase which is readily oxidized

and dissolved. Grain boundary dissolution leads to eventual breakage of entire grains

from the matrix, resulting in both ionic and colloidal Np in solution.

Based on the proposed conceptual model, a kinetic model for $NpO_2(s)$ dissolution

is developed as a two-step mechanism of $NpO_2(s)$ conversion to a hydroxide phase and

subsequent oxidation and dissolution of the hydroxide. The overall reaction is given by:

$$NpO_2(s) + xH_2O \xrightarrow{k1} NpO_2(s) \cdot xH_2O \xrightarrow{k2} (NpO_2)^+_{(aq)} + xH_2O$$
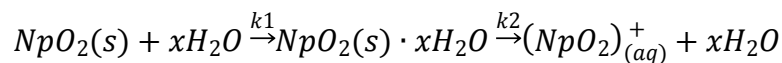
where the reaction rates of each species are described by the following set of first-order

differential equations:

$$\frac{d[NpO_2(s)]}{dt} = -k_1[NpO_2(s)]$$

$$\frac{d[NpO_2(s) \cdot xH_2O]}{dt} = k_1[NpO_2(s)] - k_2[NpO_2(s) \cdot xH_2O]$$

$$\frac{d[(NpO_2)^+_{(aq)}]}{dt} = k_2[NpO_2(s) \cdot xH_2O]$$

These equations are solved numerically, with full solutions presented in Supporting Information.

The initial conditions for the model assume that 99.7% of total Np is in the form of

$NpO_2(s)$, while 0.3% is Np hydroxide. The model fit to two replicates of experimental

data shown in Figure 6 was obtained using values of 4.0 x10^{-7} hr^{-1} and 3.5 x 10^{-3} hr^{-1} for

k_1 and k_2, respectively, indicating that the conversion of $NpO_2(s)$ to a hydrated phase is

the rate-limiting step. The initial fraction of Np hydroxide is rapidly oxidized and

dissolved, but the extremely limited amount of highly available Np hydroxide and slow

conversion from $NpO_2(s)$ causes aqueous ^{237}Np concentrations to plateau. The

experimental observation that Np(IV) is the only solid phase oxidation state further

confirms that oxidation to Np(V) is slower than desorption of Np(V). A corollary to this

observation is that the oxidation of the hydroxide phase is more rapid than oxidation of
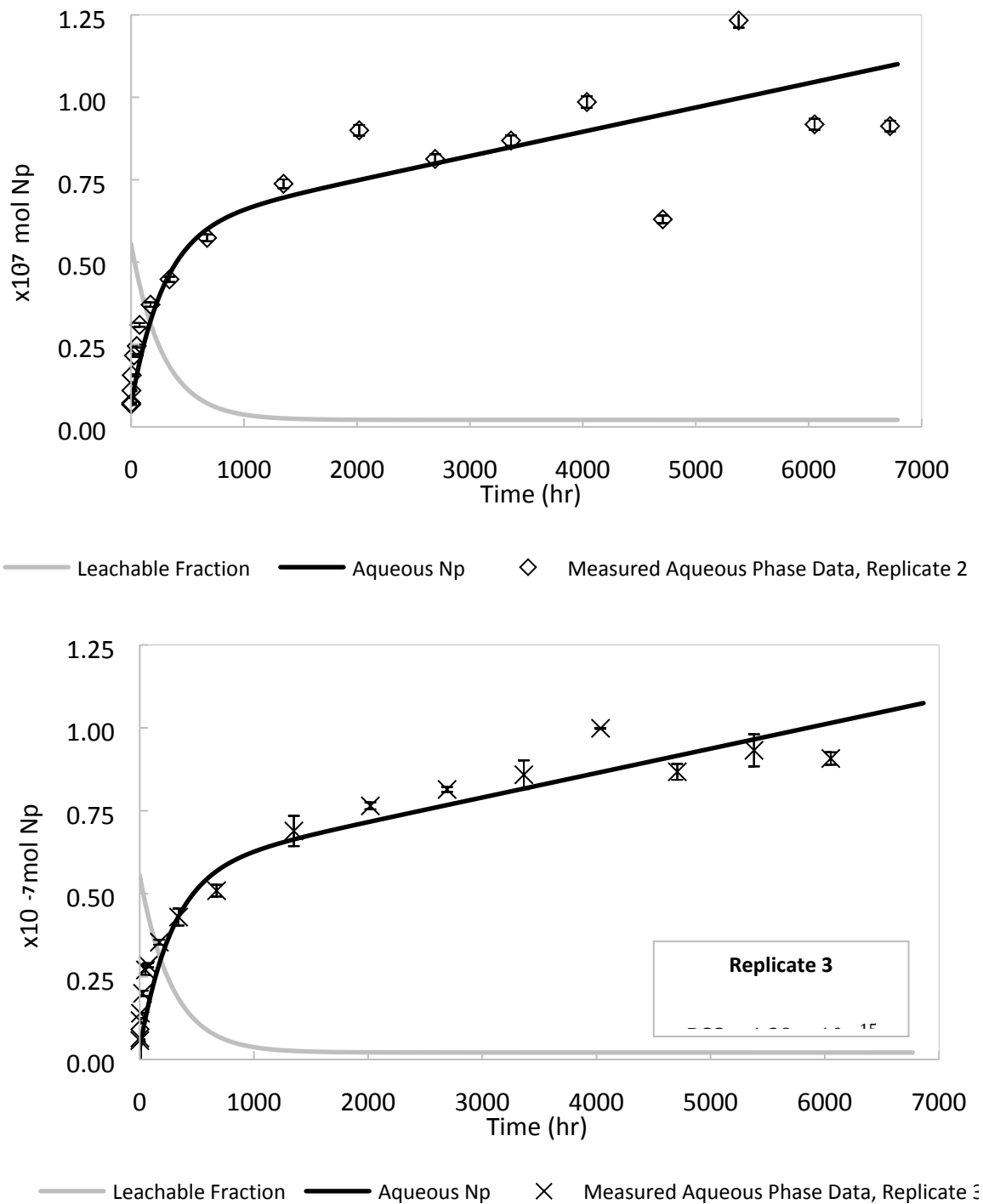
the oxide phase.

Figure 6. Kinetic fitting of aqueous unfiltered Np experimental data from two replicates of dissolution. Error bars on experimental data are shown but hidden by data points and

represent measurement error from ICP-MS. $NpO_2(s)$ fitting is not visible due to scale of graph. Residual sum of squares (RSS) calculated for each data set separately.

Conclusions

Dissolution experiments and solid phase characterization have been performed

to determine an oxidizing dissolution rate and mechanism of a nanocrystalline $NpO_2(s)$

derived from DOE legacy waste processing to inform environmental performance

assessment for actinide waste disposition. The conceptual and quantitative rate models

describe preferential dissolution of a hydroxide phase, contained within the grain

boundaries of the material, leading to fragmentation of the larger matrix and ultimately

both ionic and colloidal Np species in solution. The dissolution rate was largely

controlled by an initial rapid oxidation and dissolution of the hydroxide phase and then

limited by the slow hydration of the crystalline oxide phase. Changes to surface

features of the nanocrystalline $NpO_2(s)$ were observed using electron microscopy

techniques, revealing that the solid is preferentially dissolved at the grain boundaries,

which agreed well with conceptual models for dissolution of other nanocrystalline oxide

materials[31-33]. Measurement of colloidal Np in the aqueous phase, along with imaging

of nanometer-sized crystallites after dissolution, implied that colloid-facilitated transport

of Np may play a role in environmental mobility from nanocrystalline actinide dioxides,

as was also proposed in field-scale transport data on $NpO_2(s)$[17]. The observed

complexity of $NpO_2(s)$ dissolution indicates that thorough characterization of actinide

solid phases, particularly microstructural features such as grain boundaries, is

warranted for more accurate assessment of environmental fate and transport of

actinides. Study of the formation of grain boundaries of transuranic oxides may lead to

enhanced understanding of the dissolution mechanisms as well. Nanoscale differences

in initial environmental source terms may also help explain the large observed

differences in solubility of $NpO_2(s)$ and reveal the need for more comprehensive studies

of the formation, evolution, and potential effects of surface features on the fate of

actinides in environmental systems.

ASSOCIATED CONTENT

Supporting Information.

1 file with 4 tables, 5 figures and additional text.

AUTHOR INFORMATION

Corresponding Author

*Brian A. Powell, bpowell@clemson.edu, office (864) 656-1004

Author Contributions

The manuscript was written through equal contributions of all authors. All authors have

given approval to the final version of the manuscript.

ACKNOWLEDGMENTS

1
2
3
4
5
6
7
8
9
10
11
12
13
14
15
16
17
18
19
20
21
22
23
24
25
26
27
28
29
30
31
32
33
34
35
36
37
38
39
40
41
42
43
44
45
46
47
48
49
50
51
52
53
54
55
56
57
58
59
60

References

1.   J. Bruno and R. C. Ewing, Spent nuclear fuel, *Elements*, 2006, **2**, 343-349.

2.   J. Duffey, *Lab Scale Production of NpO2*, SRS (US). Funding organisation: US
        Department of Energy (United States), 2003.

3.   J. Duffey, *Characterization of Neptunium Oxide Generated Using the HB-Line
        Phase II Flowsheet*, SRS, 2003.

4.   T. Severynse, *Nuclear Material Processing at the Savannah River Site*,
        Westinghouse Savannah River Company, Aiken, SC (United States);
        Westinghouse Savannah River Co., Aiken, SC (United States), 1998.

5.   D. Albright and K. Kramer, Neptunium 237 and Americium: world inventories and
        proliferation concerns, *Institute for Science and International Security*, 2005,
        6060, 1-24.

6.   J. A. Cherry, W. M. Alley and B. L. Parker, Geologic Disposal of Spent Nuclear
        Fuel, *The Bridge on Emerging Issues in Earth Resources Engineering*, 2014, **44**,
        51-59.

7.   R. C. Ewing, Long-term storage of spent nuclear fuel, *Nature Materials*, 2015, **14**,
        252.

8.   V. Neck and J. Kim, Solubility and hydrolysis of tetravalent actinides,
        Radiochimica Acta, 2001, **89**, 1-16.

9.   T. Fanghänel and V. Neck, Aquatic chemistry and solubility phenomena of
        actinide oxides/hydroxides, *Pure and Applied Chemistry*, 2002, **74**, 1895-1907.

10.   J. P. Kaszuba and W. H. Runde, The aqueous geochemistry of neptunium:
        Dynamic control of soluble concentrations with applications to nuclear waste
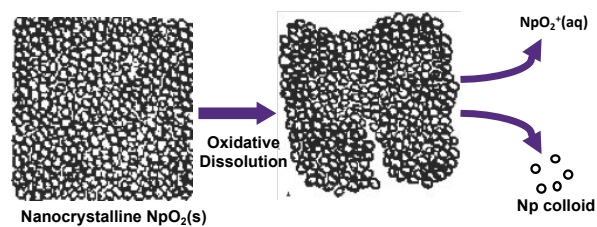   disposal, *Environmental Science & Technology*, 1999, **33**, 4427-4433.

11. R. Silva and H. Nitsche, Actinide environmental chemistry, *Radiochimica acta*, 1995, **70**, 377-396.

12. J. Morse and G. Choppin, The chemistry of transuranic elements in natural-waters, *Reviews in aquatic sciences*, 1991, **4**, 1-22.

13. G. Choppin, Actinide speciation in the environment, *Journal of Radioanalytical and Nuclear Chemistry*, 2007, **273**, 695-703.

14. T. Wu, S. Amayri, J. Drebert, L. R. V. Loon and T. Reich, Neptunium(V) Sorption and Diffusion in Opalinus Clay, *Environmental Science & Technology*, 2009, **43**, 6567-6571.

15. I. R. Triay, C. Cotter, M. H. Huddleston and D. E. Leonard, *Batch sorption results for neptunium transport through Yucca Mountain tuffs. Yucca Mountain Site Characterization Program milestone 3349*, 1996.

16. H. S. Viswanathan, B. A. Robinson, A. J. Valocchi and I. R. Triay, A reactive transport model of neptunium migration from the potential repository at Yucca Mountain, *Journal of Hydrology*, 1998, **209**, 251-280.

17. K. M. Peruski, M. Maloubier, D. I. Kaplan, P. M. Almond and B. A. Powell, Mobility of Aqueous and Colloidal Neptunium Species in Field Lysimeter Experiments, *Environmental Science & Technology*, 2018, **52**, 1963-1970.

18. D. Rai, J. Swanson and J. Ryan, Solubility of $NpO_2 \cdot xH_2O$ (am) in the presence of Cu (I)/Cu (II) redox buffer, *Radiochimica Acta*, 1987, **42**, 35-42.

19. D. Rai and J. L. Ryan, Neptunium (IV) hydrous oxide solubility under reducing and carbonate conditions, *Inorganic Chemistry*, 1985, **24**, 247-251.

20. S. Nakayama, T. Yamaguchi and K. Sekine, Solubility of neptunium (IV) hydrous oxide in aqueous solutions, *Radiochimica acta*, 1996, **74**, 15-20.

21. V. Neck, J. Kim, B. Seidel, C. M. Marquardt, K. Dardenne, M. Jensen and W. Hauser, A spectroscopic study of the hydrolysis, colloid formation and solubility of Np (IV), *Radiochimica Acta*, 2001, **89**, 439-446.

22. H. Moriyama, M. I. Pratopo and K. Higashi, The solubility and colloidal behaviour of neptunium (IV), *Science of the total environment*, 1989, **83**, 227-237.

23. R. G. Strickert, D. Rai and R. W. Fulton, 1983.

24.   S. Kim, M. Baik and K. Kang, Solubility of neptunium oxide in the KURT (KAERI Underground Research Tunnel) groundwater, *Journal of radioanalytical and nuclear chemistry*, 2009, **280**, 577-583.

25.   K. Lieser, U. Mühlenweg and I. Sipos-Galiba, Dissolution of Neptunium dioxide in aqueous solutions under various conditions, *Radiochimica Acta*, 1985, **39**, 35-42.

26.   D. J. Wronkiewicz, E. C. Buck and J. K. Bates, Grain Boundary Corrosion and Alteration Phase Formation During the Oxidative Dissolution of UO 2 Pellets, *MRS Online Proceedings Library Archive*, 1996, **465**.

27.   D. J. Wronkiewicz, J. K. Bates, S. F. Wolf and E. C. Buck, Ten-year results from unsaturated drip tests with UO2 at 90 C: implications for the corrosion of spent nuclear fuel, *Journal of Nuclear Materials*, 1996, **238**, 78-95.

28.   R. J. Finch, E. C. Buck, P. A. Finn and J. K. Bates, Oxidative corrosion of spent UO 2 fuel in vapor and dripping groundwater at 90 C, *MRS Online Proceedings Library Archive*, 1999, **556**.

29.   P. Finn, R. Finch, E. Buck and J. Bates, Corrosion mechanisms of spent fuel under oxidizing conditions, *MRS Online Proceedings Library Archive*, 1997, **506**.

30.   L. E. Thomas and R. E. Einziger, Grain boundary oxidation of pressurized-water reactor spent fuel in air, *Materials Characterization*, 1992, **28**, 149-156.

31.   C. L. Corkhill, D. J. Bailey, F. Y. Tocino, M. C. Stennett, J. A. Miller, J. L. Provis, K. P. Travis and N. C. Hyatt, Role of microstructure and surface defects on the dissolution kinetics of CeO2, a UO2 fuel analogue, *ACS applied materials & interfaces*, 2016, **8**, 10562-10571.

32.   C. L. Corkhill, E. Myllykylä, D. J. Bailey, S. M. Thornber, J. Qi, P. Maldonado, M. C. Stennett, A. Hamilton and N. C. Hyatt, Contribution of energetically reactive surface features to the dissolution of CeO2 and ThO2 analogues for spent nuclear fuel microstructures, *ACS applied materials & interfaces*, 2014, **6**, 12279-12289.

33.   J. Vandenborre, B. Grambow and A. Abdelouas, Discrepancies in thorium oxide solubility values: study of attachment/detachment processes at the solid/solution interface, *Inorganic chemistry*, 2010, **49**, 8736-8748.

34.   Peruski, Kathryn, R. Pope, M. Maloubier and B. A. Powell, Determination

of constituent concentrations in field lysimeter effluents.*Journal*, 2016.

35. M. L. Jackson, *Soil chemical analysis: Advanced course*, UW-Madison Libraries Parallel Press, 2005.

36. Y. A. Teterin, A. Y. Teterin, K. Ivanov, M. Ryzhkov, K. Maslakov, K. St N, V. Petrov and D. Enina, X-ray photoelectron spectra structure and chemical bond nature in NpO 2, *Physical Review B*, 2014, **89**, 035102.

37. B. Veal, D. Lam, H. Diamond and H. Hoekstra, X-ray photoelectron-spectroscopy study of oxides of the transuranium elements Np, Pu, Am, Cm, Bk, and Cf, *Physical Review B*, 1977, **15**, 2929.

38. B. Veal, D. Lam and H. Diamond, X-ray photoelectron spectroscopy of 5f electrons in dioxides of neptunium and plutonium, *Physica B+ C*, 1977, **86**, 1193-1194.

39. V. Neck, J. Kim and B. Kanellakopulos, Solubility and hydrolysis behaviour of neptunium (V), *Radiochimica Acta*, 1992, **56**, 25-30.

40. A. Seibert, T. Gouder and F. Huber, Reaction of neptunium with molecular and atomic oxygen: Formation and stability of surface oxides, *Journal of Nuclear Materials*, 2009, **389**, 470-478.

41. E. S. Ilton and P. S. Bagus, XPS determination of uranium oxidation states, *Surface and Interface Analysis*, 2011, **43**, 1549-1560.

42. E. S. Ilton, J.-F. Boily and P. S. Bagus, Beam induced reduction of U (VI) during X-ray photoelectron spectroscopy: the utility of the U4f satellite structure for identifying uranium oxidation states in mixed valence uranium oxides, *Surface Science*, 2007, **601**, 908-916.